Fiber-tip micro-cavity for temperature and transverse load sensing

Jun Ma, Jian Ju, Long Jin, Wei Jin,* and Dongning Wang

Department of Electrical Engineering, The Hong Kong Polytechnic University, Hong Kong, China
*eewjin@polyu.edu.hk

Abstract: A low cost fiber-optic micro-cavity interferometric sensor is presented. The micro-cavity is fabricated at the fiber tip by splicing a silica capillary to a single mode fiber and then heating/melting the capillary to form a microsphere with an internal air cavity. Applications of the micro-cavity sensor for temperature and traverse load measurements are demonstrated. The sensor has small size and good mechanical strength, and may be used in high temperature environment.

References and links

1. Y. J. Rao, "Recent progress in fiber-optic extrinsic Fabry-Perot interferometric sensors," Opt. Fiber Technol. **12**(3), 227–237 (2006).
2. V. Bhatia, K. A. Murphy, R. O. Claus, M. E. Jones, J. L. Grace, T. A. Tran, and J. A. Greene, "Optical fiber based absolute extrinsic Fabry-Perot interferometric sensing system," Meas. Sci. Technol. **7**(1), 58–61 (1996).
3. H. Y. Choi, K. S. Park, S. J. Park, U. C. Paek, B. H. Lee, and E. S. Choi, "Miniature fiber-optic high temperature sensor based on a hybrid structured Fabry-Perot interferometer," Opt. Lett. **33**(21), 2455–2457 (2008).
4. J. S. Sirkis, D. D. Brennan, M. A. Putman, T. A. Berkoff, A. D. Kersey, and E. J. Friebele, "In-line fiber etalon for strain measurement," Opt. Lett. **18**(22), 1973–1975 (1993).
5. Y. J. Rao, M. Deng, T. Zhu, and H. Li, "In-line Fabry-Perot etalons based on hollow-core photonic bandgap fibers for high-temperature applications," J. Lightwave Technol. **27**(19), 4360–4365 (2009).
6. Y. J. Rao, M. Deng, D. W. Duan, X. C. Yang, T. Zhu, and G. H. Cheng, "Micro Fabry-Perot interferometers in silica fibers machined by femtosecond laser," Opt. Express **15**(21), 14123–14128 (2007).
7. T. Wei, Y. Han, Y. Li, H.-L. Tsai, and H. Xiao, "Temperature-insensitive miniaturized fiber inline Fabry-Perot interferometer for highly sensitive refractive index measurement," Opt. Express **16**(8), 5764–5769 (2008).
8. J. Villatoro, V. Finazzi, G. Coviello, and V. Pruneri, "Photonic-crystal-fiber-enabled micro-Fabry-Perot interferometer," Opt. Lett. **34**(16), 2441–2443 (2009).
9. Y. Zhu, and A. Wang, "Miniature fiber-optic pressure sensor," IEEE Photon. Technol. Lett. **17**(2), 447–449 (2005).
10. V. B. Braginsky, M. L. Gorodetsky, and S. P. Vyatchanin, "Thermo-refractive noise in gravitational wave antennae," Phys. Lett. A **271**(5-6), 303–307 (2000).
11. Y. Zhu, K. L. Cooper, G. R. Pickrell, and A. Wang, "High-temperature fiber-tip pressure sensor," J. Lightwave Technol. **24**(2), 861–869 (2006).
12. M. LeBlanc, S. T. Vohra, T. E. Tsai, and E. J. Friebele, "Transverse load sensing by use of pi-phase-shifted fiber Bragg gratings," Opt. Lett. **24**(16), 1091–1093 (1999).
13. M. Silva-Lopez, C. Li, W. N. MacPherson, A. J. Moore, J. S. Barton, J. D. Jones, D. Zhao, L. Zhang, and I. Bennion, "Differential birefringence in Bragg gratings in multicore fiber under transverse stress," Opt. Lett. **29**(19), 2225–2227 (2004).
14. C. Jewart, K. P. Chen, B. McMillen, M. M. Bails, S. P. Levitan, J. Canning, and I. V. Avdeev, "Sensitivity enhancement of fiber Bragg gratings to transverse stress by using microstructural fibers," Opt. Lett. **31**(15), 2260–2262 (2006).
15. T. Geernaert, G. Luyckx, E. Voet, T. Nasilowski, K. Chah, M. Becker, H. Bartelt, W. Urbanczyk, J. Wojcik, W. De Waele, J. Degrieck, H. Terryn, F. Berghmans, and H. Thienpont, "Transversal load sensing with fiber Bragg gratings in microstructured optical fibers," IEEE Photon. Technol. Lett. **21**(1), 6–8 (2009).
16. Y. Liu, L. Zhang, and I. Bennion, "Fibre optic load sensors with high transverse strain sensitivity based on long-period gratings in B/Ge co-doped fibre," Electron. Lett. **35**(8), 661–663 (2002).
17. J. Xu, X. Wang, K. L. Cooper, and A. Wang, "Miniature all-silica fiber optic pressure and acoustic sensors," Opt. Lett. **30**(24), 3269–3271 (2005).

1. Introduction

Optical fiber Fabry-Perot interferometers (FPIs) have been widely used for sensing temperature, strain, pressure, and etc [1–8]. Strain sensors have been made by inserting two

pieces of single mode fiber (SMF) into a tube to form an FPI by the air-gap between two air-silica interfaces [2]. FPIs have also been fabricated by splicing a short segment of hollow-core fiber or hollow-core photonic bandgap fiber between two sections of SMFs [4, 5]. Recently, FPIs were fabricated by ablating a groove in a SMF by use of a femtosecond laser, and were studied for strain [6] and refractive index measurement [7]. However, the aforementioned methods for FPI fabrication need stringent alignment between the two fibers inserting into the tube, careful cleaving, and/or the use of expensive lasers. In addition, the multiple splices or surface imperfection (i.e., ablation) would degrade the mechanical strength of the fiber, which is important for many practical applications.

In this paper, we demonstrate a low cost fiber-tip FPI-like micro-cavity sensor for high temperature and transverse-load measurement. This sensor is fabricated by splicing a silica capillary to a SMF and then fusing (heating/melting) the capillary to form a microsphere with an internal air-cavity. In the entire fabrication process, only a fusion splicer is needed. The fabrication of the sensor is reported in section 2, and the results of temperature and transverse load measurements are presented respectively in sections 3 and 4, followed by a brief summary of the findings.

2. Fabrication of micro-cavity

Figure 1 shows the fabrication process of the fiber-tip micro-cavity. Firstly, a conventional SMF (SMF28) is spliced to a capillary with an outer diameter $D = 126$ μm and an inner diameter $d = 75$ μm, by use of the normal-splice-program of an Ericsson FSU-975 fusion splicer. The splice joint is then moved horizontally by use of a translation stage so that the position of the splicer's electrodes offsets the splice joint by L. Afterward, the splicing parameters are adjusted to increase the arc discharge current to ~20 mA and the discharge time to ~1 s, the arc discharge is then applied to the capillary section, as shown in Fig. 1(b). During the discharge, the temperature reaches the softening/melting point of silica and the capillary is separated into two parts. One part is a microsphere with an internal air-cavity and is firmly attached to the end of the SMF, as shown in Figs. 1(c) and 1(e). For the example shown in Fig. 1(e), the value of L used is ~ 400 μm; the length (d^*) of the air cavity is estimated, by using an optical microscope, to be ~ 84 μm, and the thickness (t) of the outer silica wall (between surfaces 2 and 3) is ~ 30 μm. The length and the shape of the air-cavity may be adjusted by the offset distance L. In the whole process, only a fusion splicer is used and no additional alignment procedure is needed.
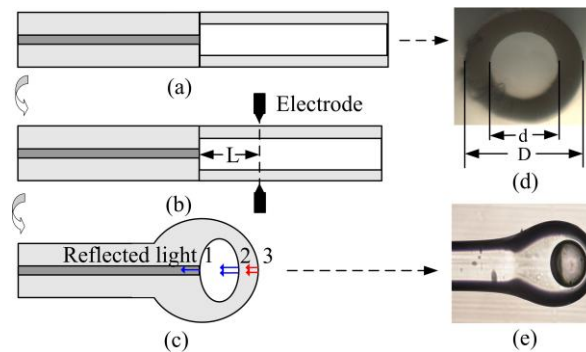

Fig. 1. Fabrication of the micro-cavity. (a) Splice a silica capillary to a SMF; (b) heat and melt the capillary to form an air cavity (L: distance from electrode to the SMF end); (c) a sketch showing the fiber-tip micro-cavity; microscope image of (d) capillary cross-section and (e) micro-cavity.

Considering that the reflectivity of the silica/air interface is less than 3.5%, the higher-order reflections from these surfaces may be ignored [8]. As a result, three reflected waves may be collected and guided back along the SMF: one is from the end of the SMF (1), the

other two are from the inner and outer surfaces of the silica wall (2, 3), as indicated in Fig. 1(c). These three reflected beams interfere and the return light intensity will be modulated [9].

Figure 2(a) shows the measured reflection spectrum of the micro-cavity shown in Fig. 1(e). The spectrum was measured using the setup shown in Fig. 3. A broadband source (BBS) and an optical spectrum analyzer (OSA) are connected to the two input ports of a 3-dB coupler. The fiber-tip micro-cavity senor is connected to the output port. The BBS consists of five individual super-luminescent light emitting diodes (LEDs) with wavelength ranging from 1200 nm to 1700 nm and the spectrum of the BBS is shown in Fig. 3(b). The spectrum of the micro-cavity shows an interference fringe visibility of ~15 dB. The fringes are the results of the coherent mixing of the three reflected waves. By immersing the fiber-tip into a refractive index liquid with $n = 1.4$, the reflection from the outer silica surface (3) is minimized and the reflections from the two inner surfaces of the air-cavity become dominant. The reflection spectrum is changed to Fig. 2(b). The interference fringes in Fig. 2(b) are not exactly sinusoidal, probably due to the divergence of the beam when traveling outside of the SMF fiber and the residual reflection from the outer silica surface. Nevertheless, from Fig. 2(b), we may estimate the effective length d^* of the air-cavity, by using the relationship $\Delta\lambda = \lambda^2 / 2n_{air}d^*$, to be $d^* = 76$ μm, where $\Delta\lambda$ denotes the fringe wavelength spacing, n_{air} (≈ 1) is the refractive index of air.
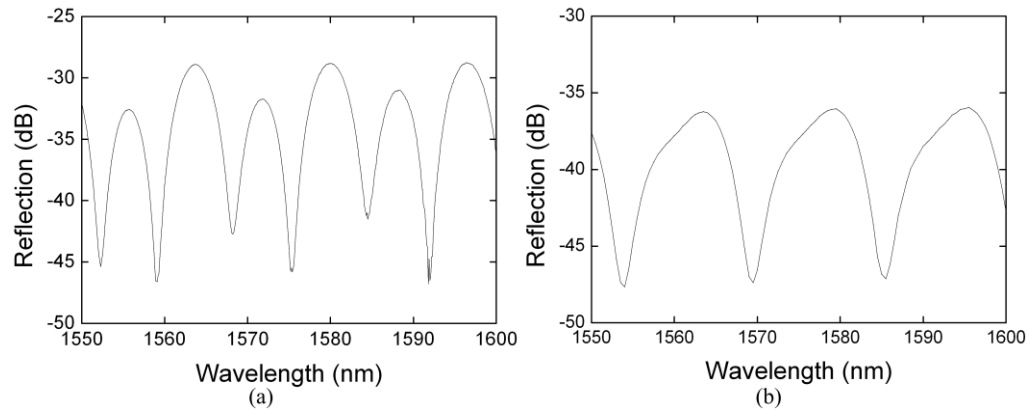

Fig. 2. Reflection spectrum of the micro-cavity shown in Fig. 1(e). The fiber-tip is placed (a) in air and (b) in a liquid with refractive index of 1.4. The spectrums were normalized by the source spectrum.
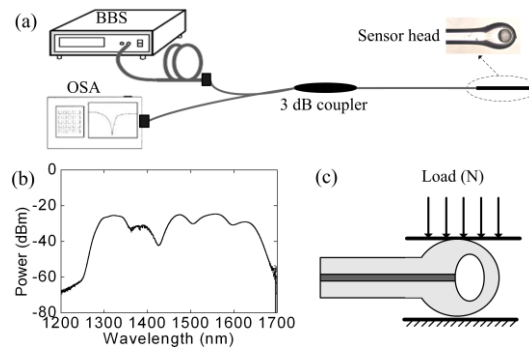

Fig. 3. (a) Setup for measuring the reflection spectrum of the micro-cavity sensor; (b) spectrum of the BBS; (c) setup for transverse load test.

By changing the offset distance L, micro-cavities with different cavity lengths can be fabricated. Figure 4(a) shows the measured air-cavity lengths with an optical microscope for several micro-cavities made with different offset distances. The cavity length increases in

general with the offset distance L, but the slope becomes small for $L < 200$ μm. Figure 4(b) shows the fringe wavelength spacing around 1525 nm for micro-cavities with different air-cavity lengths. The calculated results (the solid curve) are close to the ones estimated by using the microscope image (the dots). The discrepancy may arise from the refraction of spherical shape of the cavity as well as the inaccuracy of microscope measurement, which was found to vary considerably with the position of the focal plane.
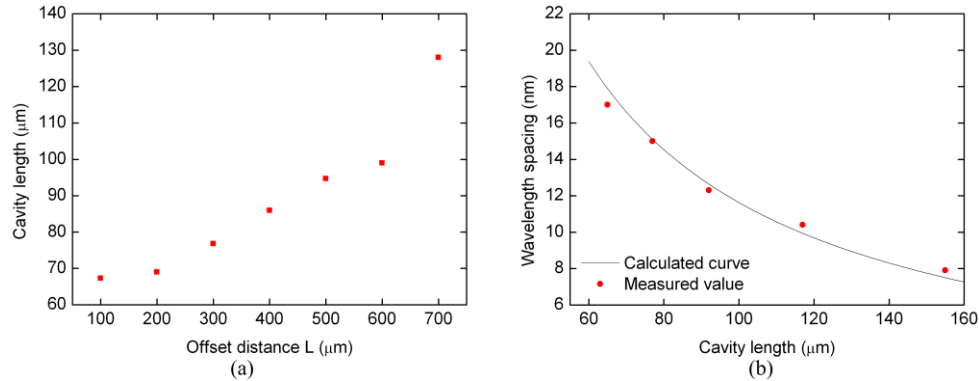

Fig. 4. (a) Dependence of air-cavity length on offset distance L; (b) relationship between fringe wavelength spacing and air-cavity length.

Figure 5 shows the microscope images of the micro-cavities fabricated with $L = 300$, 400, and 700 μm. In addition to the air-cavity length, the thickness of the silica wall t also has an increasing trend with L. However, when the offset distance L is smaller than 200 μm, the air cavity is difficult to be reduced further. The reason might be that for smaller air cavity, the effect of inner air-pressure, which tends to increase the air cavity size during the arc discharge process, becomes dominant and prevents the further reduction of the air cavity.
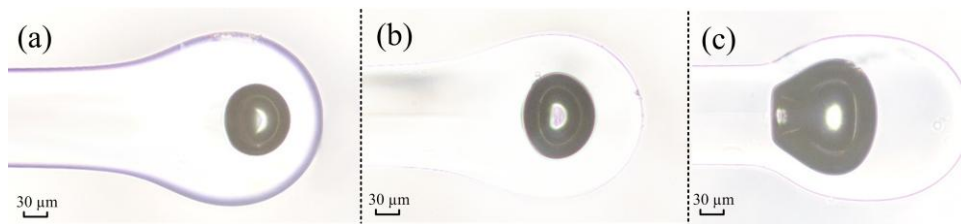

Fig. 5. Micro-cavities fabricated with different offset distances L. (a) 300 μm; (b) 400μm; (c) 700μm.

3. Response to temperature

3.1 Experimental test

The temperature characteristics of a fiber-tip micro-cavity sensor were measured by using a similar system shown in Fig. 3. The fiber-tip was placed horizontally in a furnace. The heating rate of the furnace was set to be 15 °C/min, and the temperature was raised in steps of 100 °C and maintained for about 30 min at each step to make sure the temperature in the furnace have stabilized. After the temperature reached 1000 °C, the heating process was stopped and the temperature was decreased by natural cooling. The cooling process was also in steps of 100 °C, and the temperature was maintained for about 30 min. In order to test the repeatability, the heating and cooling cycle was repeated for 3 times. The fiber-tip was not immersed into the refractive index liquid and the fringes observed are due to the interference of the three reflected waves (three-wave mode) with a reflection spectrum similar to the one shown in Fig. 2(a).

Figure 6(a) shows the temperature response of the sensor from room temperature to 1000 °C. The wavelength shifts to longer wavelength with the increase of temperature. Figure 6(b)

shows the measured wavelength-temperature relationship of the sensor for the two dips around wavelength 1513 nm and 1522 nm respectively. The sensitivities of the two dips are respectively ~8.7 and 7.6 pm/°C. The sensor worked well up to temperature ~1000 °C, and showed a good repeatability with a maximum discrepancy ~ 0.2 nm for the dip wavelengths between up and down temperature cycles. Before the start of the cycling measurement, the micro-cavity sensor was firstly heated to 1000 °C and maintained the temperature for several hours. Within the first hour, the fringe dip wavelengths were found to shift ~ 0.4 nm to longer wavelength and the dip intensities varied slightly, i.e., 0.28 dB for dip 1 and 0.56 dB for dip 2. The dip intensity variations are believed to be related to the shifts of the dip wavelength, as can be seen from Fig. 6(a). No obvious change of the interference spectrum was observed in the remaining several hours of annealing.
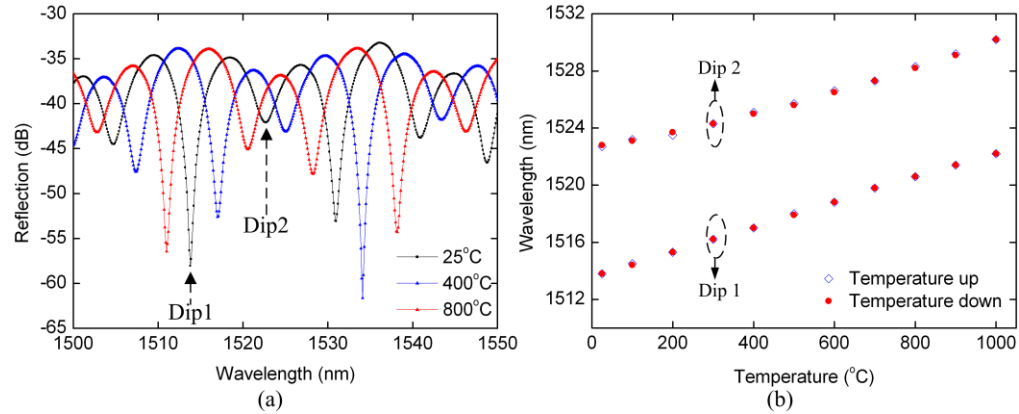

Fig. 6. (a) Shift of reflection spectrum with temperature; (b) dip wavelengths as functions of temperature. The cavity length d^* and the silica wall thickness t are respectively 63 µm and 44 µm.
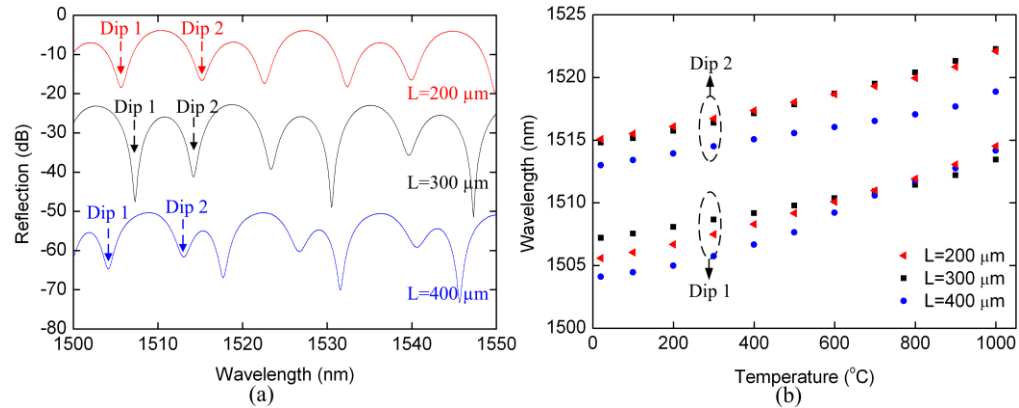

Fig. 7. (a) Spectrum of micro-cavity sensors fabricated with different offset distances L. The spectrums are offset vertically for the purpose of easy observation. The actual spectrums are all around the level of - 30 dB; (b) Dip wavelengths as function of temperature for cavities made with different offset distances L.

Figure 7 shows the spectrums of micro-cavity sensors fabricated with different offset distances L = 200, 300 and 400 µm. The temperature sensitivity of the sensor was studied by monitoring the wavelengths corresponding to specific dips (i.e., dips 1 and 2 as indicated in Fig. 7(a)) in the interference spectrum. The measured sensitivities of the dip wavelengths for three different sensors are listed in the Table 1. The cavity length d^* and the silica wall

thickness t in Table 1 were estimated by use of an optical microscope. The smaller value of t for $L = 300$ μm may be caused by the instability of the arc-discharges.

Table 1. Temperature characteristics of micro-cavity sensors fabricated by different offset distances

Offset distance L (μm)		200	300	400
Cavity length d^* (μm)		66	74	81
Outside silica wall thickness t (μm)		46	45	59
Temperature sensitivity (pm/°C)	Dip 1	9.9	6.0	10.4
	Dip 2	6.9	7.7	5.5

3.2 Discussion

As mentioned in sections 2 and 3.1, the fringes shown in Figs. 2(a), 6(a) and 7(a) are due to interference of three waves, which are respectively reflected from the three surfaces as shown in Fig. 1(c). For the reflected waves associated with the internal air-cavity, the thermally induced refractive index change of air may be negligible [3] and the thermal expansion of the cavity length would then play a main role in the temperature sensitivity. An increase of the temperature will elongate the cavity length d^*, which increases $\Delta\phi = 4\pi d^* / \lambda$ and leads to the red shift of the dip wavelength. The wavelength shift of the two-wave interference pattern to temperature is given as follows,

$$\frac{\Delta\lambda}{\lambda} = (\frac{\Delta L}{L} + \frac{\Delta n}{n}) = \varepsilon + \kappa \tag{1}$$

where ε is the thermal expansion coefficient and κ is the thermo-optic coefficient. For pure silica, $\varepsilon = 5.5 \times 10^{-7}$ and $\kappa = 1.0 \times 10^{-5}$ [10]. If only the interference between the two reflected waves from the air-cavity (i.e., surfaces 1 and 2) is considered, the sensitivity of the dip wavelength (around 1513 nm) to temperature is theoretically estimated to be ~0.83 pm/°C. This is significantly different from the measured sensitivity, which is almost an order of magnitude higher than the FPI reported previously [8]. If the fringe shift for the interference between reflected waves from surfaces 2 and 3 is considered, the temperature sensitivity is ~15.96 pm/°C. As a result, we believe the high temperature sensitivity of the micro-cavity sensor is mainly due to the thermally induced refractive index change of silica wall, which affects both the phase difference between reflected waves from surface 3 and surface 2, and the reflected waves from surface 3 and surface 1.

However, the above discussion based on the two-wave interference cannot accurately predict the significantly different temperature sensitivities of the different interference dips. To better understand the thermal behavior of the micro-cavity sensor, we consider the three waves interference model. The light intensity at the sensor output may be expressed as below [11],

$$I \propto |E|^2 = \left| E_1 - E_2 \cdot \exp(\frac{4\pi}{\lambda} n_{air} d^*) + E_3 \cdot \exp\left[\frac{4\pi}{\lambda}(n_{silica} t + n_{air} d^*)\right]\right|^2$$

$$= E_1{}^2 + E_2{}^2 + E_3{}^2 - 2E_1 E_2 \cdot \cos(\frac{4\pi}{\lambda} n_{air} d^*) - 2E_2 E_3 \cdot \cos(\frac{4\pi}{\lambda} n_{silica} t) \tag{2}$$

$$+ 2E_1 E_3 \cdot \cos\left[\frac{4\pi}{\lambda}(n_{silica} t + n_{air} d^*)\right]$$

where, E_1, E_2, and E_3 are respectively the amplitudes of the three reflected waves, d^* is the length of the air cavity, t is the thickness of the outside silica wall, λ is light wavelength, and

n_{air} and n_{silica} are respectively the refractive indexes of air and silica. The negative sign before E_2 is due to the π-phase shift of reflection at surface 2.

By curve fitting the interference pattern (e.g., Fig. 2a), the value of E_1, E_2, E_3, d^* and t can be acquired. Then the temperature sensitivity of the micro-cavity sensor can be estimated theoretically. Taking the micro-cavity sensor fabricated with offset distance $L = 400$ μm as an example, the air-cavity length and thickness of the silica wall are found to be $d^* = 83$ μm and $t = 58$ μm, very close to the results obtained from the microscope as in Table 1. The calculated sensitivities are respectively 10.6 pm/°C and 6.5 pm/°C for wavelength dips around 1503 and 1513 nm, close to the measured values in Table 1.

To ensure unambiguous and absolute temperature measurement, the values of d^* and/or t need to be demodulated or recovered accurately. This in principle can be done by curve fitting the measured spectrums but may be impractical for field applications due to dependence on appropriate initial conditions and the large number of variables which results in computational ineffectiveness [11]. The spherical reflection surface instead of standard plane surface may also induce inaccuracy and need special models which may further increase the demodulation complexity.

The sensor demodulation may be significantly simplified if only two-beams involved in the interference process. This can be achieved by reducing reflection from the outer silica surface by for example immersing or imbedding the fiber-tip into a higher index material or simply blackening or roughening the outer silica surface to reduce reflection. Then, only interference of the two beams reflected from two air-cavity surfaces remains. This also significantly reduces the temperature sensitivity of the sensor, which may be beneficial to some applications. An example of such applications is presented in section 4.

4. Response to transverse load

4.1 Experimental test

Transverse load detection has important applications in structural health monitoring. Compared with the strain sensing, the transverse load is in the direction perpendicular to the fiber axis. In the past years, transverse load sensing have been realized by using fiber Bragg grating (FBG) [12–15] or long period grating (LPG) [16].

Transverse load measurement was carried with a fiber-tip micro-cavity sensor with an air cavity length of ~100 μm and an outer silica wall thickness (i.e., the separation between surfaces 2 and 3) of ~ 60 μm. The measurement setup is similar to that shown in Fig. 3, and the measured reflection spectrums without transverse loading are shown in Fig. 8. Figure 8(a) shows the reflection spectrum where all the three reflected waves are involved in the interference process, while Fig. 8(b) is the spectrum when the outer surface of the tip (surface 3) was blackened by applying matt black aerosol paint. The blackening is preferred over surface roughening, which might comprise the mechanical strength of the sensor.
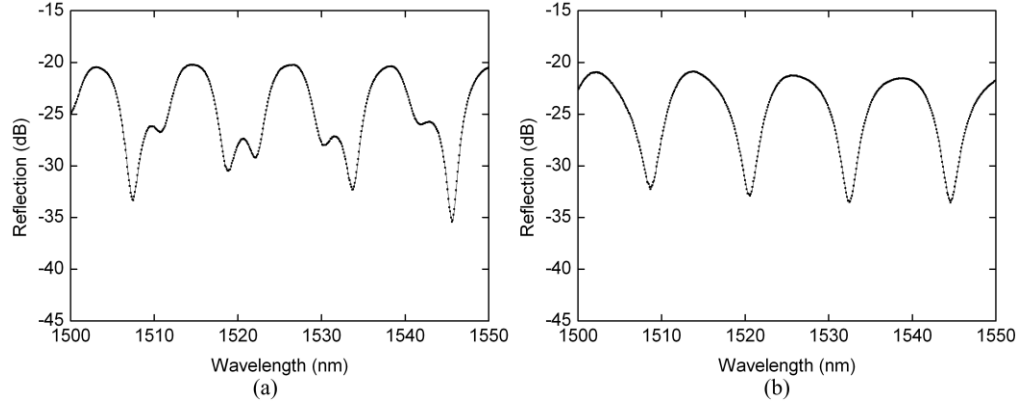
Fig. 8. Reflection spectrum of a fiber-tip micro-cavity. The fiber-tip is (a) without blackening process and (b) after blackening process. No transverse load is applied.

The blackened sensor head was placed between two parallel metal plates as shown in Fig. 3(c). Different transverse loads were applied perpendicularly to the upper plate and the fringe dip wavelength is recorded. With the increase of the transverse load, the cavity elongates longitudinally, which causes the phase difference between the two beams ($\Delta\varphi = 4\pi d^* / \lambda$) to increase. This makes the reflected spectrum shift to longer wavelength. As shown in Fig. 9(a), the sensor shows a transverse load sensitivity of ~ 1.37 nm/N. In the experiment, we also find that the transverse load sensitivity of the micro-cavity sensor depends on the cavity shape and cavity center position in the fiber tip. By more careful design, the sensitivity may be further enhanced. Working is continuing along this direction.

The temperature response of the micro-cavity sensor was also tested and shown in Fig. 9 (b). The temperature sensitivity is ~ 2.1 pm/°C. It should be emphasized that this is the sensitivity of the air-cavity, i.e., the interference between the reflected waves from surfaces 1 and 2, and the reflections from surface 3 is minimized by blackening the surface 3 as mentioned previously. For such an air-cavity, the thermally induced refractive index change of air may be negligible and the thermal expansion of the cavity length would play a main role in the temperature sensitivity. An increase of the temperature will elongate the cavity length d^*, leading to the red shift of the dip wavelength. The low sensitivity of the micro-cavity sensor to temperature would be beneficial to temperature insensitive transverse load sensing.
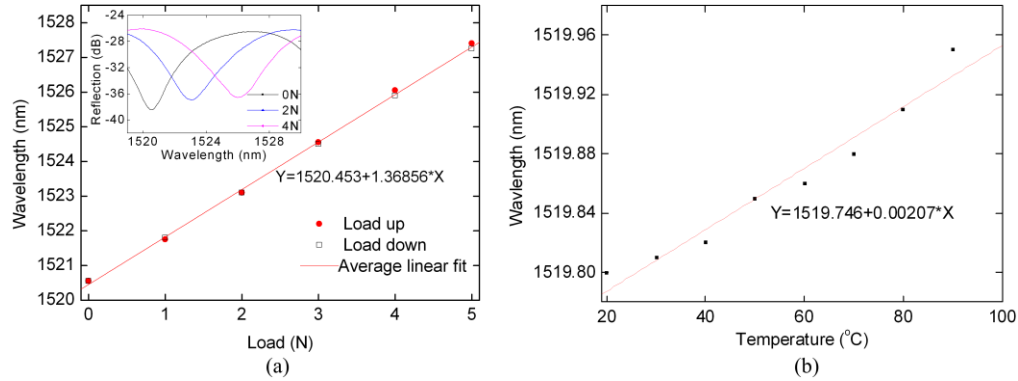

Fig. 9. (a) Transverse load sensitivity of the micro-cavity sensor in the range of 0 - 5 N; insert: reflection spectrum for different transverse loads; (b) temperature sensitivity of the micro-cavity sensor.

4.2 Discussion

Compared with the FBG or LPG based transverse load sensors that have the highest transverse load sensitivity of ~1 nm/N [16], the micro-cavity transverse load sensor shows a higher sensitivity of 1.37 nm/N. If no temperature compensation is used, the error caused by temperature cross-sensitivity will be about 1.5×10^{-3} N/°C. This may be neglected in applications in which large transverse load is involved. The micro-cavity sensor is similar to a point-contact load sensor and the high sensitivity is believed to be caused by the large pressure created by the load on the small contacting area. Hence, appropriate package is important for the senor to maintain the high transverse load sensitivity in practical applications.

5. Conclusion

In summary, a compact fiber-tip micro-cavity sensor was fabricated by use of the electric arc discharge to melt a section of capillary which is spliced to a single mode fiber end. The micro-cavity sensor demonstrated an interference fringe visibility exceeding 15 dB. The sensor can work a three-wave interference mode or a two-wave interference mode. In the three-wave mode, a temperature sensor with good repeatability up to 1000 °C was demonstrated. In the two-wave mode, a transverse load sensor with a high sensitivity of ~ 1.37 nm/N and a low temperature sensitivity of ~ 2.1 pm/°C was demonstrated. The sensor is tiny and works in a reflection mode, and hence may be used in space-limited environment.

In addition, refractive index sensing may be implemented by filling the air-cavity with the target liquid through for example a hole dilled transversely [7]. The micro-cavity sensor may also be used as a sensitive pressure detector if the outer silica wall could be made thinner using for example wet etching [17]. The good high temperature performance and mechanical strength means that the micro-cavity sensor may be used as gas/liquid pressure sensor in harsh (high temperature) environment. We are currently working along this direction.

Acknowledgements